Grain refinement in additively manufactured ferritic stainless steel by in situ inoculation using pre-alloyed powder

Citation for the original published paper (version of record):
Durga, A., Pettersson, N., Malladi, S. et al (2021). Grain refinement in additively manufactured ferritic stainless steel by in situ inoculation
using pre-alloyed powder. Scripta Materialia, 194.
http://dx.doi.org/10.1016/j.scriptamat.2020.113690

(article starts on next page)

Scripta Materialia 194 (2021) 113690

Contents lists available at ScienceDirect

Scripta Materialia

journal homepage: www.elsevier.com/locate/scriptamat

Grain refinement in additively manufactured ferritic stainless steel by *in situ* inoculation using pre-alloyed powder

A. Durga[a], Niklas Holländer Pettersson[a], Sri Bala Aditya Malladi[b], Zhuoer Chen[b], Sheng Guo[b], Lars Nyborg[b], Greta Lindwall[a,*]

[a] Department of Materials Science and Engineering, KTH Royal Institute of Technology, Brinellvägen 23, SE-100 44 Stockholm, Sweden
[b] Industrial and Materials Science, Chalmers University of Technology, SE-41296 Gothenburg, Sweden

ARTICLE INFO

Article history:
Received 19 November 2020
Revised 15 December 2020
Accepted 18 December 2020

Keywords:
Laser Powder-Bed Fusion
Columnar-to-equiaxed transition
Inoculation
Solidification
Ferritic stainless steels

ABSTRACT

For ferritic stainless steels, TiN has effectively been used as an inoculant to produce equiaxed grain structures in casting and welding. However, it is not established whether TiN would be an effective inoculant in additive manufacturing. In this study, the effectiveness of TiN as an inoculant in a ferritic stainless steel processed by laser powder-bed fusion is studied. An alloy without Ti is fabricated and compared to an alloy designed to form a high amount of TiN early during solidification. The work shows that the presence of TiN provides general grain refinement and that TiN-covered oxide particles are effective in enabling columnar-to-equiaxed transition in certain regions of the meltpool. The applied approach of pre-alloying powders with inoculant-forming elements offers a straightforward route to achieving fine, equiaxed grain structures in additively manufactured metallic materials. It also shows how oxygen present during the process can be utilized to nucleate effective inoculating phases.

Additive Manufacturing (AM) of metallic materials using powder-bed fusion based techniques, typically results in columnar grain structures at the mesoscale due to directional heat flow during solidification [1]. Such grain structures may be susceptible to cracking [2,3] and result in anisotropic properties, thereby complicating design of components with reliable and predictable mechanical behavior. Based on solidification theory [4], the transition from columnar to equiaxed grain structure can be inducedby reducing the thermal gradient at the solidification front or increasing the cooling rate, which in turn increases the solidification front velocity. Additionally, it is also possible topromote equiaxed grain growth by modifying the alloy composition to increase the constitutional supercooling or by introducing large amounts of heterogeneous nucleation sites (inoculating phases withlow undercooling for nucleating the solid). These approaches have been utilized in AM [5] by altering the process parameters such as scan speed, beam shape, beam diameter, scan rotation [6–8], and by using inoculants to change the solidification conditions [3,9–11]. Successful grain refinement in different material systems by modifying the feedstock powder through *ex situ* addition of inoculant-forming nanoparticles have been reported on [3,9]. However, the practical difficulties of how to incorporate these nanoparticles into the feedstock powder and safety concerns should be recognized. Pre-alloying the powder with inoculant-forming elements, on the other hand, allows for *in situ* formation of the inoculating phase during printing [10,11].

Recently, Karlsson et al. [12] reported on a ferritic stainless steel AISI441 produced by L-PBF from an unmodified feedstock powder having excellent mechanical properties (>679 MPa yield strength) attributed to a very fine grain size (<1.8 μm). For this class of steels, TiN is reported to be an effective ferrite inoculant in both casting and welding [13,14], given the low lattice mismatch between TiN and ferrite, and favorable interfacial energies. However, it is not well-established whether TiN is an effective inoculant for ferrite for AM. The purpose of this study is hence to explore if grain refinement can be achieved under L-PBF conditions by *in situ* formation of TiN inoculants during the AM process with ferritic steels as a model alloy.

Two ferritic stainless steel model alloy powders based on the AISI 441 composition, one without Ti (Ti-free), and one with higher amount of Ti (Ti-high) than AISI 441 to delineate the effect of Ti, were designed to be nitrogen gas atomized. Computational thermodynamics based on the Calphad method [15] was applied for the model alloy design and the Ti-high composition was selected based on: (i) maximum solubility of N in the liquid phase (~ 0.1

* Corresponding author.
E-mail address: gretal@kth.se (G. Lindwall).

https://doi.org/10.1016/j.scriptamat.2020.113690
1359-6462/

Table 1
Measured chemical compositions (wt.%) of powder and as-built ferritic stainless steels without and with Ti.

Alloy	Cr	Ti	N	C	Ni	Si	Nb	Mn	Co	V	Mo	O	Cu	P	Al	Fe
Ti-free powder	17.7	<0.01	0.079	0.017	0.27	0.43	<0.01	0.83	0.02	0.04	0.05	0.057	<0.01	0.011	0.007	Bal.
Ti-free as-built	17.8	<0.01	0.08	–	0.25	0.6	<0.01	0.79	0.02	0.04	0.04	0.068	<0.01	0.012	<0.01	Bal.
Ti-high powder	18.7	0.85	0.14	0.021	0.12	0.52	0.27	0.92	0.01	0.06	0.04	0.038	0.01	0.012	0.023	Bal.
Ti-high as-built	19.1	0.73	0.097	–	0.15	0.77	0.29	0.86	0.02	0.07	0.04	0.046	0.01	0.011	<0.01	Bal.

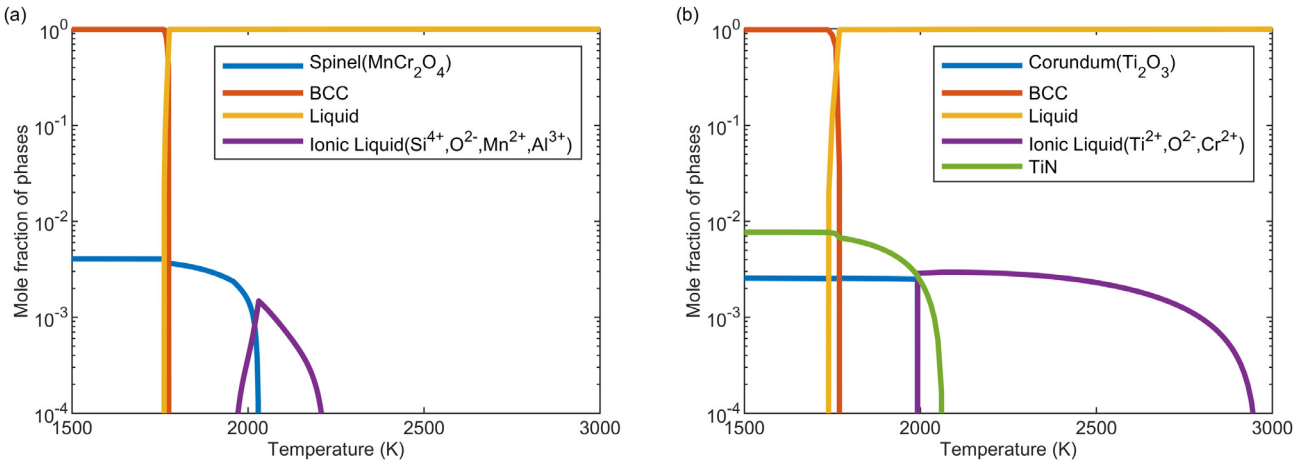

Fig. 1. Phase fractions at equilibrium as a function of temperature calculated for the (a) Ti-free and (b) Ti-high as-built compositions listed in Table 1 (the major elements in the oxygen-rich and intermetallic phases are indicated in the legend): different types of high temperature oxides are predicted to form for the two compositions. TiN and Ti-rich corundum are predicted to form during solidification before ferrite for the Ti-high composition.

mass%) at typical gas atomization temperatures, and a tradeoff between (ii) maximizing the amount of inoculating phase, TiN, stable at the solidification temperature of the ferrite phase, while (iii) limiting the stability of the intermetallic phases Laves ($Fe_2(Ti,Nb)$) and σ-phase that becomes stable below 970°C in this case. The Laves and σ-phase are both undesired due to their embrittling effect on the mechanical properties [16,17]. The amounts of minor elements were specified to be as low as possible.

The two alloy powders were fabricated by means of nitrogen gas atomization by Kanthal AB and were sieved to 10 – 45 µm size range. Cubes with dimensions 5 mm x 5 mm x 5 mm were built by means of L-PBF in an EOS M100 machine. The following process parameters were used: 110 W, 800 mm/s, 80 μm hatch distance, 20 μm layer thickness. The printing atmosphere was argon and the oxygen levels were maintained at >0.1vol% during the process. Pressure in the printing chamber was 1 atm at 20 °C and the build plate was not pre-heated. The resulting densities were greater than 99.9% for both materials. The powder compositions and the compositions of the as-built materials, measured by ICP-OES and LECO analysis, are shown in Table 1.

Figure 1 shows the equilibrium phase fraction versus temperature for both Ti-free and Ti-high as-built compositions calculated using Thermo-Calc Software TCFE Steels/Fe-alloys database version 10 [18]. Trace elements were not included in the calculations. For the Ti-free composition, ferrite is the major solid phase expected to form, with a small fraction of ionic liquid consisting of Si^{4+}, Mn^{2+}, Al^{3+}, O^{2-}, which is predicted to solidify as spinel phase. For the Ti-high composition, TiN is expected to form during solidification before ferrite formation. Also, Ti-rich ionic liquid is expected to solidify as Ti-rich corundum. In casting, it has been demonstrated that TiN itself preferentially nucleates on complex titanium-containing oxides (TiO_x) like Ti_2O_3 Ti_3O_5, Ti_2O [14–18], resulting in TiN-covered particulate complexes, which act as effective ferrite inoculants to produce equiaxed grain structures. Hence, the oxygen pickup during atomization, powder handling, and L-PBF process,can be expected to lead to corundum formation, which could favor TiN nucleation in the Ti-high composition.

The as-built microstructures were characterized using electron microscopy. Samples for scanning electron microscopy (SEM) were sectioned parallel to the build direction and prepared by grinding and polishing to 1 µm diamond finish, followed by final polishing using colloidal alumina and silica solutions (50 and 40 nm-sized particles, respectively). The grain structure was analyzed by electron backscattered diffraction (EBSD) in a focused ion beam (FIB) Nova 600 nanolab dual beam field emission gun (FEG) FIB-SEM. The EBSD measurements were performed at 20 kV using a Symmetry CMOS EBSD detector from Oxford Instruments. The EBSD data was processed using MTEX v5.2.8 crystallographic Toolbox and Matlab R2018b. Complementary backscattered electron imaging was performed using a Jeol 7800F FEG-SEM. The particles in the materials were further studied by transmission electron microscopy (TEM). For the Ti-high material, FIB lamella was lifted from a fine-grained region; in the Ti-free material the sample was extracted by random positioning. The FIB lamellae were thinned to electron transparency by rough milling at 30 kV followed by final milling at 5 kV. TEM was performed in a Jeol 2100F FEG-TEM operated at 200 kV. Chemical analysis was performed by energy dispersive spectroscopy (EDS) using a X Max^N windowless EDS detector.

Comparing the builds fabricated from the Ti-free and Ti-high powders, it is clear that the same build strategy and process parameters result in very different microstructures as shown in Figure 2. The Ti-free material (Figure 2a) has a microstructure with larger grains extending over several build layers and a <001> fiber texture parallel to the build direction (Figure 2c). The Ti-high material (Figure 2b) has a finer microstructure with columnar and equiaxed regions outlining the separate melt pools and the texture seems more randomized (Figure 2d). Though both materials display lognormal grain size distributions (Figure 2e), the mean grain size decreases from 14.2 ± 1.1 μm to 1.2 ± 0.01 μm (95% confi-

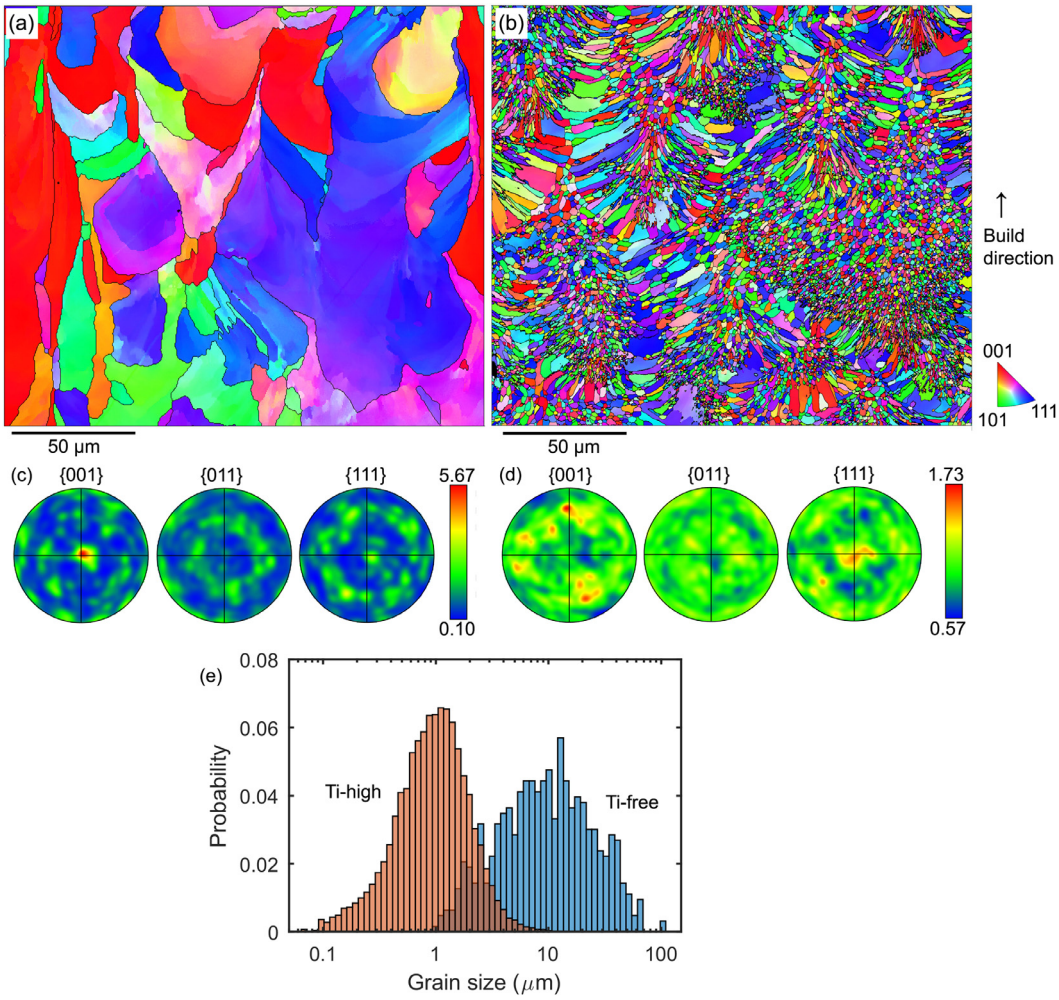

Fig. 2. EBSD inverse pole figure colored maps showing the microstructure in the (a) Ti-free and (b) Ti-high materials; build direction pole figures for the (c) Ti-free and (d)Ti-high materials; and (e) the grain size distribution of the two materials (note that both the pole figures and the grain size distribution are based on larger data sets than the ones shown in (a) - (b)).

dence) by the addition of Ti and the whole distribution is shifted to smaller grain sizes. There is evidently significant grain refinement in the Ti-high case.

To better understand the grain refinement mechanism, possible inoculating particles in the two different microstructures were analyzed by SEM and TEM. The Ti-free material contains a fine dispersion of particles evenly distributed within the grains (Figure 3a). STEM HAADF and EDS show that these particles are spherical Cr-Si-Mn-Al-containing oxides (Figure 3e, g and h). The Ti-high material is found to have a different distribution of particles in the fine-grained regions compared to the columnar regions (Figure 3b). In the fine-grained regions, particles are seen distributed randomly within the grains (Figure 3c) and a majority of them have diameters greater than 20-30 nm (histogram in Figure 4). In the columnar region, particles are also seen. They are, however, finer with a majority sized 20 nm or smaller (Figure 3d, histogram in Figure 4). From STEM HAADF imaging (Figure 3f) of a fine-grained region, it is seen that the particles are cuboidal with irregular shapes and appear in most cases to consist of clusters of a few particles. A STEM EDS line measurement (Figure 3j) over a particle cluster (Figure 3i) shows that the core is Ti-Al-rich oxide, and the outer parts have a higher concentration of Ti and N. It should be noted, however, that the energy of Ti L and N K lines are overlapped in EDS, and N in the presence of Ti has therefore been estimated by peak deconvolution comparing with the Ti L/K line ratio. Since N is detected only in the outer parts of the particle where the O content is low, these particle clusters presumably have a Ti-Al-oxide-core and outer layer of TiN.

Hence, there is a clear difference between the Ti-free and Ti-high materials, both in terms of grain structures and second phase particles. Since the main difference between the two compositions is the amount of Ti (Table 1), the effect of adding Ti and the formation of TiN *in situ* can be delineated through a comparison of the two structures. There are three aspects that elucidate this effect: the presence of different types of particles in the Ti-free and Ti-high materials, the different sizes of particles in the columnar and equiaxed regions of the Ti-high material, and finally the observed grain structure at the meltpool scale.

Firstly, consistent with the fact that there is oxygen present already in the powder (Table 1), a fairly uniform distribution of oxygen-rich particles throughout the build for both Ti-free (Cr-Si-Mn-Al-O) and Ti-high (Ti-Al-O) materials can be seen (Figure 3). This is expected for L-PBF processed materials, where nano-oxides are typically found owing to oxygen from the feedstock powder and L-PBF process conditions [19]. For the Ti-free material, the thermodynamic calculations (Figure 1.a) predict the spinel phaseto be stable. It was not possible to confirm the crystal structure and it is not clear based on the morphology whether the oxides are spinel [19]. Through previous studies [13,20], it has been shown that oxide particles are not effective nucleation sites for ferrite

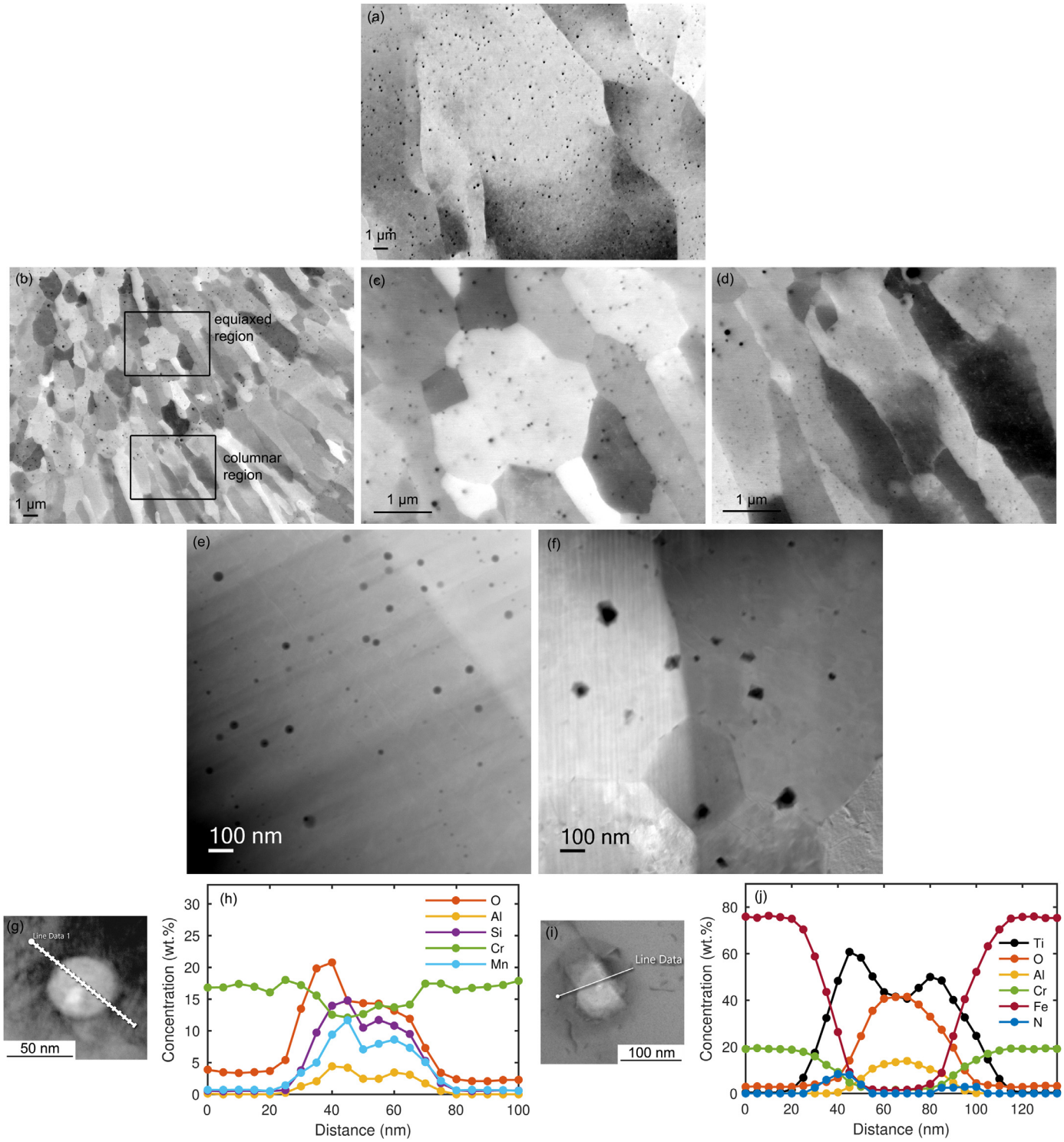

Fig. 3. Distribution, morphology and chemistry ofparticles: SEM backscattered electron images showing (a) homogeneous distribution of particles in the Ti-free material and (b) a different distribution of particles found in columnar and equiaxed zones of the Ti-high material, as seen clearly in the zoomed-in images of (c) equiaxed region and (d) columnar region; STEM HAADF images showing the particle morphology in (e) Ti-free and (f) Ti-high materials (equiaxed zone); STEM-EDS line scans of (g) the spherical particles in Ti-free material and (h) the irregular shaped particles found in Ti-high material (equiaxed zone).

as a very high undercooling is required. Therefore, there is no inoculating effect of oxygen-rich particles on the grain structure for the Ti-free material. On the other hand, the Ti-high material seems to have TiN encapsulating Ti-Al-O particles, which can act as inoculants. This is consistent with thermodynamic calculations (Figure 1b), which show that TiN and Ti-rich corundum are stable up to temperatures close to 2000 K. Therefore, the observed particle clusters (Figure 3f) have most likely formed by nucleation of TiN on corundum particles early in the solidification process, since the peak temperatures during L-PBF can reach 2500-3000 K [21–23]. In fact, these particle clusters are very similar to TiO_x/TiN clusters reported in the case of casting [24,25] which act as inoculants, although at a much finer scale in this study, suggesting that TiN preferentially nucleated on the oxides rather than homogeneously

in the liquid [26]. Accordingly, the presence of oxygen, which can be difficult to completely avoid during powder handling and L-PBF processing, seems to be advantageous in enabling the *in situ* formation of TiN inoculants for grain refinement.

Next, the implications of different particle sizes in the columnar and equiaxed regions of the Ti-high material (Figure 3c and d) on nucleation and growth of new grains are analyzed. At L-PBF conditions, the undercooling required for heterogeneous nucleation and growth of equiaxed grains has to be viewed in relation to the undercooling for epitaxial growth of columnar grains from the underlying, already solidified material, which is the competing mechanism. The undercooling for columnar growth (driven by thermal gradient) can be anywhere between a few degrees to a few tens of degrees, depending on the process parameters [14,27]. Based on nucleation theory, Nakajima et al. [20] calculated the critical nucleus size of TiN for effective nucleation of ferrite to 7.4 nm and validated it experimentally. The undercooling required for further growth of nuclei into equiaxed grains is, however, dependent on the inoculant particle size on which they nucleate and can be very high if the particle size is very small. According to Greer et al. [28], the undercooling required for the growth (ΔT_{fg}) of nuclei that form on the inoculant surface as a function of the inoculant particle size can be calculated as:

$$\Delta T_{fg} = \frac{4\sigma_{SL}}{\Delta S_v\, d}$$

where σ_{SL} is the solid-liquid interfacial energy, ΔS_v is the entropy of fusion per unit volume and d is the particle size. Taking σ_{SL} as 0.045 J m^{-2} and ΔS_v as 7.2646•10^5 J m^{-3} K^{-1} calculated using theThermo-Calc Software v2020b TCFE Steels/Fe-alloys database version 10 [18], the undercooling as a function of the inoculant particle size is shown in Figure 4. In line with these calculations, the particles in the equiaxed region seem to be more effective for nucleation and growth of ferrite than the much smaller particles in the columnar region due to lower undercooling, also in comparison with the undercooling required for columnar growth (Figure 4). To predict the columnar-to-equiaxed transition more accurately, the local thermal conditions also need to be known.

Finally, considering the grain structure at the meltpool scale, a polycrystalline structure in the Ti-free material is observed where the grains themselves in many cases span several layer thicknesses.

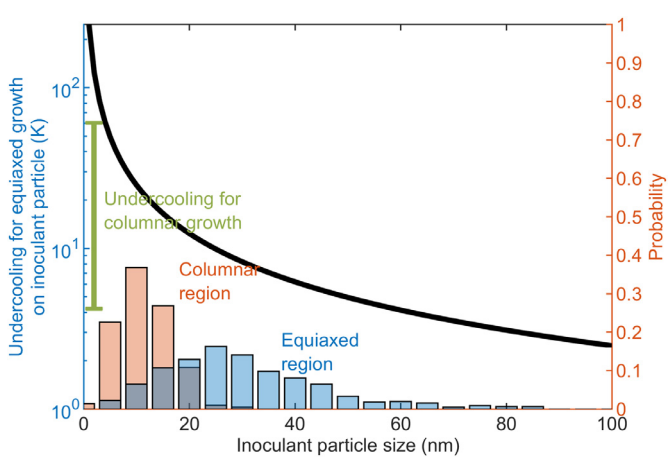

Fig. 4. Undercooling for equiaxed growth on inoculant particle as a function of the particle size (black curve with y-axis on the left): The particles in the equiaxed region of Ti-high material are larger than those in the columnar region (given by the two histograms showing the probability of the inoculant particle size as indicated by the y-axis on the right, based on measurements from SEM images) and therefore more favorable for nucleating equiaxed grains, when compared with the undercooling required for columnar growth (rough range indicated by the green line segment).

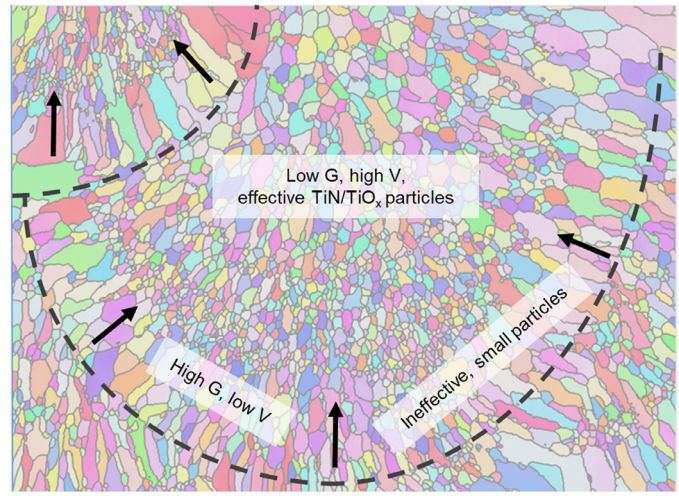

Fig. 5. Schematic showing the conditions and the distribution of particles at different parts of the meltpool that influence the grain morphology.

This is a typical structure observed in L-PBF processed materials and is mainly dependent on the local thermal gradients, which can be influenced by the scan speed and scan rotation [7,29]. Regarding the texture, it is also interesting to note that the <001> fiber texture, as observed for the Ti-free material (Figure 2c), is found in ferritic stainless steels produced by strip casting [30] with a high directionality in heat transfer which resembles the present situation. The more randomized texture (Figure 2d) in the Ti-high material further indicates that the solidification conditions have been modified. In the Ti-high material, firstly, columnar-to-equiaxed transition in morphology is seen within each meltpool. This can be explained by the presence of TiN-oxide particle clusters, present in larger sizes in the equiaxed regions and smaller sizes in the columnar regions. Furthermore, local thermal gradient (G) is expected to be higher and solidification velocity (V) is expected to be lower at the bottom of the meltpool compared to the top, which favors columnar growth [31]. This is depicted in a schematic in Figure 5. Moreover, there is significant refinement in grain size in the Ti-high material compared to the Ti-free material in both columnar and equiaxed regions (Figure 2a and b). Refinement of the columnar grains is potentially due to them nucleating on the fine, equiaxed structure at the top of previous meltpools in the underlying solid layer.

In summary, the efficacy of *in situ* formed TiN as an inoculant for ferritic stainless steel in L-PBF was demonstrated by comparing the structures of a Ti-free base alloy and an alloy with Ti. Though fine oxygen-rich particles were present in both cases, they were of different types and in the case of the alloy with Ti, covered by TiN, which enabled grain refinement and columnar-to-equiaxed transition. TiN, which has traditionally been used as an inoculant in casting and welding, may therefore also be used in L-PBF, further aided by the presence of oxygen-rich inclusions. This paves the way for design of new powders pre-alloyed with alloying elements that form inoculating phases *in situ* during AM. Furthermore, the oxygen level of the powder and possible pick-up during the process may also be utilized as a design strategy to nucleate suitable inoculating phases.

Declaration of Competing Interest

The authors declare that they have no known competing financial interests or personal relationships that could have appeared to influence the work reported in this paper.

Acknowledgements

This study was performed within the strategic innovation program Metalliska Material through the project Design of novel materials and processes for next generation additive manufacturing (DEMA), financed by the Swedish Governmental Agency for Innovation Systems (VINNOVA), Formas and Energimyndigheten. The industrial project partners Höganäs AB, Kanthal AB, Quintus Technologies AB, Sandvik Materials Technology and Jernkontoret are acknowledged for valuable input. Roger Berglund, Kanthal AB, is acknowledged for materials supply, chemical analysis and valuable discussions. LN and GL also acknowledge support from VINNOVA via LIGHTer Academy.

References

[1] F. Yan, W. Xiong, E.J. Faierson, Materials (Basel) 10 (2017) 1260.
[2] N.J. Harrison, I. Todd, K. Mumtaz, Acta Mater 94 (2015) 59–68.
[3] J.H. Martin, B.D. Yahata, J.M. Hundley, J.A. Mayer, T.A. Schaedler, T.M. Pollock, Nature 549 (2017) 365–369.
[4] J.D. Hunt, Mater. Sci. Eng. 65 (1984) 75–83.
[5] D. Zhang, A. Prasad, M.J. Bermingham, C.J. Todaro, M.J. Benoit, M.N. Patel, D. Qiu, D.H. StJohn, M.A. Qian, M.A. Easton, Metall. Mater. Trans. A. 51 (2020) 4341–4359.
[6] N. Raghavan, R. Dehoff, S. Pannala, S. Simunovic, M. Kirka, J. Turner, N. Carlson, S.S. Babu, Acta Mater 112 (2016) 303–314.
[7] S. Sun, K. Hagihara, T. Nakano, Mater. Des. 140 (2018) 307–316.
[8] T.T. Roehling, R. Shi, S.A. Khairallah, J.D. Roehling, G.M. Guss, J.T. McKeown, M.J. Matthews, Mater. Des. 195 (2020) 109071.
[9] X.P. Li, G. Ji, Z. Chen, A. Addad, Y. Wu, H.W. Wang, J. Vleugels, J. Van Humbeeck, J.P. Kruth, Acta Mater 129 (2017) 183–193.
[10] K.V. Yang, Y. Shi, F. Palm, X. Wu, P. Rometsch, Scr. Mater. 145 (2018) 113–117.
[11] A.B. Spierings, K. Dawson, T. Heeling, P.J. Uggowitzer, R. Schäublin, F. Palm, K. Wegener, Mater. Des. 115 (2017) 52–63.
[12] D. Karlsson, C. Chou, N. Holländer Pettersson, T. Helander, P. Harlin, M. Sahlberg, G. Lindwall, J. Odqvist, U. Jansson, Addit. Manuf. (2020), doi:10.1016/j.addma.2020.101580.
[13] B.L. Bramfitt, Metall. Trans. 1 (1970) 1987–1995.
[14] V. Villaret, F. Deschaux-Beaume, C. Bordreuil, J. Mater, Process. Technol. 233 (2016) 115–124.
[15] H. Lukas, S.G. Fries, B. Sundman, Computational thermodynamics: the Calphad method, Cambridge university press, 2007.
[16] M.P. Sello, W.E. Stumpf, Mater. Sci. Eng. A. 527 (2010) 5194–5202.
[17] T.J. Nichol, A. Datta, G. Aggen, Metall. Trans. A. 11A (1980) 573–585.
[18] J.-O. Andersson, T. Helander, L. Höglund, P. Shi, B. Sundman, Calphad. 26 (2002) 273–312.
[19] F. Yan, W. Xiong, E. Faierson, G.B. Olson, Scr. Mater. 155 (2018) 104–108.
[20] K. Nakajima, H. Hasegawa, S. Khumkoa, M. Hayashi, Metall. Mater. Trans. B. 34B (2003) 539–547.
[21] W. Huang, Y. Zhang, J. Manuf. Process. 42 (2019) 139–148.
[22] P. Bian, J. Shi, X. Shao, J. Du, Int. J. Adv. Manuf. Technol. 104 (2019) 3867–3882.
[23] U. Scipioni, A.J. Wolfer, M.J. Matthews, J.R. Delplanque, J.M. Schoenung, Mater. Des. 113 (2017) 331–340.
[24] Y. Hou, G. Cheng, Metall. Mater. Trans. B. 50 (2019) 1322–1333.
[25] Y. Hou, G. Cheng, H. Cheng, Metall. Mater. Trans. B. 51 (2020) 709–721.
[26] J. Fu, Q. Nie, W. Qiu, J. Liu, Y. Wu, Mater. Charact. 133 (2017) 176–184.
[27] S.S. Babu, J.W. Elmer, J.M. Vitek, S.A. David, Acta Mater 50 (2002) 4763–4781.
[28] A.L. Greer, Phil. Trans. R. Soc. Lond. A. 361 (2003) 479–495.
[29] T. Ishimoto, S. Wu, Y. Ito, S. Sun, H. Amano, T. Nakano, ISIJ Int 60 (2020) 1758–1764.
[30] H.T. Liu, Z.Y. Liu, Y.Q. Qiu, G.M. Cao, C.G. Li, G.D. Wang, Mater. Charact. 60 (2008) 79–82.
[31] J.P. Oliveira, A.D. Lalonde, J. Ma, Mater. Des. 193 (2020) 1–12.